machines

MDPI

Article

An Autonomous Fluoroscopic Imaging System for Catheter Insertions by Bilateral Control Scheme: A Numerical Simulation Study

Gregory Y. Ward †, Dezhi Sun † and Kenan Niu *

Robotics and Mechatronics Group (RAM), University of Twente, Drienerlolaan 5, 7522 NB Enschede, The Netherlands; g.y.ward@student.utwente.nl (G.Y.W.); dezhi.sun@utwente.nl (D.S.)

* Correspondence: k.niu@utwente.nl

† These authors contributed equally to this work.

Abstract: This study presents a bilateral control architecture that links fluoroscopic image feedback directly to the kinematics of a tendon-driven, three-joint robotic catheter and a 3-DoF motorised C-arm, intending to preserve optimal imaging geometry during autonomous catheter insertion and thereby mitigating radiation exposure. Forward and inverse kinematics for both manipulators were derived via screw theory and geometric analysis, while a calibrated projection model generated synthetic X-ray images whose catheter bending angles were extracted through intensity thresholding, segmentation, skeletonisation, and least-squares circle fitting. The estimated angle fed a one-dimensional extremum-seeking routine that rotated the C-arm about its third axis until the apparent bending angle peaked, signalling an orthogonal view of the catheter's bending plane. Implemented in a physics-based simulator, the framework achieved inverse-kinematic errors below 0.20% for target angles between 20° and 90°, with accuracy decreasing to 3.00% at 10°. The image-based angle estimator maintained a root-mean-square error $\leq 3\%$ across most of the same range, rising to 6.4% at 10°. The C-arm search consistently located the optimal perspective, and the combined controller steered the catheter tip along a predefined aortic path without collision. These results demonstrate sub-degree angular accuracy under idealised, noise-free conditions and validate real-time coupling of image guidance to dual-manipulator motion; forthcoming work will introduce realistic image noise, refined catheter mechanics, and hardware-in-the-loop testing to confirm radiation-dose and workflow benefits.

Keywords: bilateral control; automated catheter insertion; surgical robotics; collaborative robotics

check for updates

Academic Editor: Jiangjian Xiao

Received: 28 April 2025
Revised: 29 May 2025
Accepted: 4 June 2025
Published: 6 June 2025

Citation: Ward, G.Y.; Sun, D.; Niu, K. An Autonomous Fluoroscopic Imaging System for Catheter Insertions by Bilateral Control Scheme: A Numerical Simulation Study. *Machines* **2025**, *13*, 498. https://doi.org/10.3390/machines13060498

Copyright: © 2025 by the authors. Licensee MDPI, Basel, Switzerland. This article is an open access article distributed under the terms and conditions of the Creative Commons Attribution (CC BY) license (https://creativecommons.org/licenses/by/4.0/).

1. Introduction

Automation within medical procedures is continuously advancing, driven by the goal of increasing procedural precision, reducing inherent risks, and safeguarding healthcare professionals from exposure to potentially harmful conditions [1]. Its rapid integration into surgical practices has become indispensable due to consistent, precise, and repeatable performance [2,3], while robotic assistance further mitigates physical strain on surgeons and radiation exposure risks in imaging-guided interventions [4].

Surgical environments frequently involve complex medical apparatus that demand considerable expertise for intricate calibration and precise positioning [5]. Even minor misalignments may compromise procedural efficiency and outcomes, emphasizing the

value of seamless coordination between surgeons and device operators. Similar challenges have been reported in the design of flexible instruments for endoscopic procedures, where accurate 3D shape analysis is essential for safe and effective navigation [6]. Fluoroscopy exemplifies such equipment, extensively used across minimally invasive and interventional radiological procedures [7]. By employing X-rays for real-time imaging, fluoroscopy assists in navigating instruments within the patient's body [8] and is typically mounted on a mobile, highly maneuverable C-Arm to enhance coverage and procedural accuracy [9]. However, it poses substantial risks from ionizing radiation exposure [10], which can lead to skin injuries or long-term carcinogenic effects for patients [11], while also threatening the long-term health of surgeons through cumulative exposure [12,13]. Moreover, operating the C-Arm's complex kinematics manually is time-consuming, especially when re-establishing the optimal imaging perspective, which prolongs surgeries and increases radiation doses [14,15].

Although complete elimination of radiation in fluoroscopy-guided procedures is infeasible, automation has the potential to reduce radiation exposure; the magnitude will depend on workflow integration and system latency. The field of minimally invasive surgery, notably aortic catheter insertion procedures, has gained significant advantages from robotic solutions that permit remote catheter navigation, thereby lowering radiation exposure for the surgeon [16]. However, most existing systems still rely on separate operators for each robotic device, presenting both safety and coordination challenges if one operator attempts to handle multiple devices simultaneously [17].

Recent developments in endovascular robotics show that commercially deployed platforms—most notably Corindus's *CorPath GRX* and Hansen Medical's *Magellan*—already enable radiation-shielded, joystick-driven catheter navigation from a remote cockpit [18,19]. These systems still depend on a scrub-side assistant to swing the fluoroscopic C-arm, preventing true imaging–motion synchrony and limiting tele-presence. Emerging work on automatic C-arm repositioning—ranging from the self-driving *CIARTIC Move* mobile arm to learning-based view-planning networks that infer target angles directly from 2-D images [20]—begins to close this loop; however, current solutions either require pre-operative CT or markers or cannot track the continuously deforming shaft of a flexible catheter in real time. At the systems level, cooperative multi-robot architectures that couple imaging and manipulation remain largely confined to simulation benches or single-arm demos, with no bilateral control of both imaging and actuation reported in vivo [21,22]. This persistent gap motivates the cooperative bilateral framework proposed here.

During fluoroscopy-guided catheterisation the team remains exposed to ionising radiation because a scrub-side assistant must manually steer the C-arm and the surgeon must mentally coordinate a tendon-driven catheter robot with that moving imager. To eliminate this two-fold burden, we develop an advanced bilateral control scheme that streams real-time X-ray images into a controller driving both a 3-DoF robotic catheter and a 3-DoF C-arm so that the fluoroscope autonomously re-aligns with each catheter motion while concentrating the beam on the region of interest (quantitative dosimetry is reserved for future work). The framework combines (i) analytic kinematics that map joint angles to catheter centre-line shape, (ii) a calibrated projection model of the C-arm that generates synthetic radiographs of the catheter and surrounding vasculature, and (iii) image-processing pipelines that retrieve the catheter's bending angle and orientation—vital inputs for the bilateral controller. As a forward-looking extension, we prototype a fully autonomous insertion routine that follows patient-specific centre-lines along predefined navigation paths, reducing reliance on operator skill and foreshadowing entirely hands-free workflows. The main contributions are threefold: (1) the first closed-loop, bidirectional control law synchronising catheter motion with autonomous C-arm repositioning; (2) a hybrid

physics–projection simulator that blends finite-element catheter mechanics, calibrated X-ray rendering, and the above insertion routine for in silico experimentation; and (3) quantitative validation showing inverse-kinematic percentage errors $\leq 0.2\%$ for bending angles 20–90° (rising to 3.0% at 10°) and an image-based angle-estimator RMSE $\leq 3\%$ over the same range, establishing a baseline for forthcoming hardware-in-the-loop trials.

The paper outline is as follows: Section 2 details the kinematics, projection model, and image pipeline; Section 3 derives the bilateral control algorithm; Section 4 presents simulation validation, including the autonomous insertion study; Section 5 discusses limitations, dosimetry plans, and translational pathways; Section 6 concludes the study.

2. Methods

The Methods Section lays out this study's theoretical foundations and core methodologies. It begins by outlining the kinematics of the C-Arm and flexible catheter, showing how forward and inverse kinematics can be derived for each device. It then covers the mathematical model for the fluoroscopic projection and details the image processing techniques for estimating catheter bending angles. These elements collectively form the framework that enables coordinated control of both the C-Arm and the catheter.

2.1. C-Arm Manipulation

2.1.1. Forward Kinematics

We model the C-Arm part of the system as a 3-DOF robotic manipulator. A diagram of said manipulator is given in Figure 1.

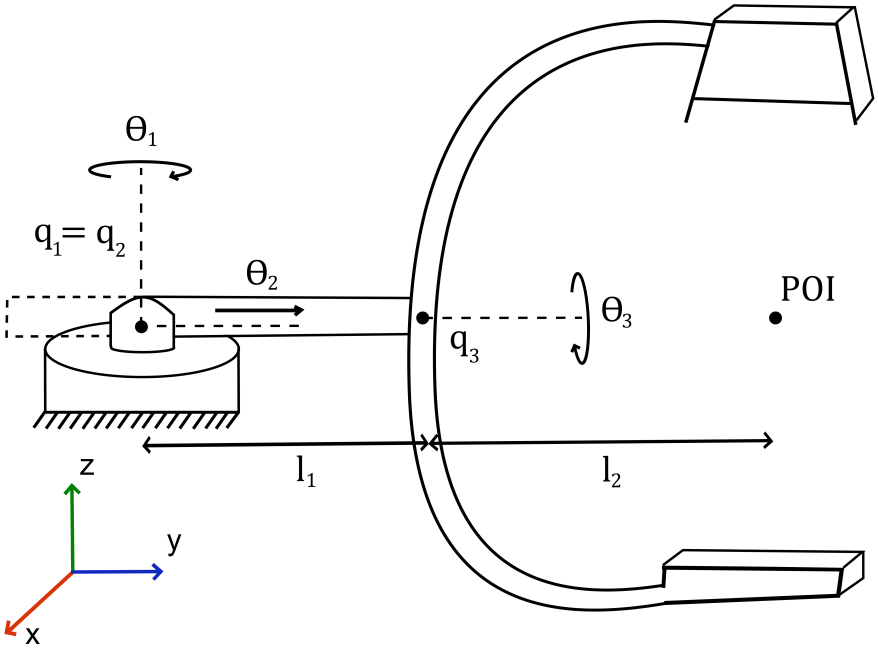


Figure 1. A diagram of the proposed C-Arm manipulator defining all relevant parameters, where θ_1: in-plane rotation of the C-arm, θ_2: radial prismatic slide, and θ_3: axial roll of the X-ray source/detector.

The application of screw theory allows for the full transformation, from the base to the end-effector of the manipulator, to be described by Equation (1).

$$g_{\mathrm{st}}(\theta) = e^{\hat{\xi}_1\theta_1} e^{\hat{\xi}_2\theta_2} e^{\hat{\xi}_3\theta_3} g_{\mathrm{st}}(0) \tag{1}$$

$\hat{\xi}_{1,2,3}$ are the corresponding 4×4 screw-axis twists, and $g_{st}(0)$ is the home homogeneous transform.

We can now evaluate Equation (1) as

$$g_{\text{st}}(\theta) = \begin{bmatrix} R(\theta) & p(\theta) \\ 0_{1\times 3} & 1 \end{bmatrix} \tag{2}$$

In Equation (2), $R(\boldsymbol{\theta})$ and $p(\boldsymbol{\theta})$ are the rotation matrix and translation vector extracted from $g_{st}(\boldsymbol{\theta})$, in which $R \in \mathbb{R}^{3\times 3}$ and $p \in \mathbb{R}^3$. To simplify representation let us define $c_i = \cos(\theta_i)$ and $s_i = \sin(\theta_i)$. We can then express $R(\theta)$ as

$$R(\theta) = \begin{bmatrix} c_1c_3 & -s_1 & c_1s_3 \\ c_3s_1 & c_1 & s_1s_3 \\ -s_3 & 0 & c_3 \end{bmatrix} \tag{3}$$

and $p(\theta)$ as

$$p(\theta) = \begin{bmatrix} -s_1(l_1 + l_2 + \theta_2) \\ c_1(l_1 + l_2 + \theta_2) \\ 0 \end{bmatrix} \tag{4}$$

l_1, l_2 are the fixed link lengths; (p_x, p_y) and (p_{x0}, p_{y0}) are the current and home end-effector coordinates in the base xy-plane . The full transformation from base to end-effector is now completely described by Equation (2).

2.1.2. Inverse Kinematics

Inverse kinematics are derived using geometric analysis methods. The first joint of the C-Arm has rotational movement fixed in the x-y plane. The second joint of the C-Arm actuates a prismatic translation within the x-y plane. An abstraction is given in Figure 2.

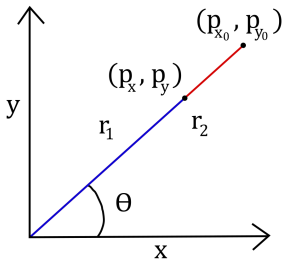


Figure 2. Abstraction of motion of joint 2.

Using polar coordinates, the angle of the first joint is straightforward to determine. Without derivation:

$$\theta_1 = \arctan \frac{p_y}{p_x} \tag{5}$$

For some angle θ, the difference in the magnitude of the end-effector in the current and zero configuration gives the joint angle θ_2.

The joint angle θ_2 is simply the difference in radii.

$$\theta_2 = r_2 - r_1 = \sqrt{p_{x_0}^2 + p_{y_0}^2} - \sqrt{p_x^2 + p_y^2} \tag{6}$$

Here, $r_1 = \sqrt{p_{x0}^2 + p_{y0}^2}$ and $r_2 = \sqrt{p_x^2 + p_y^2}$; hence, $\theta_2 = r_2 - r_1$.

2.2. Roboticising a Flexible Catheter

2.2.1. Forward Kinematics

The forward kinematics of the flexible catheter are derived differently from that of the C-Arms. Two joints shall have their homogeneous transformations determined via screw theory, whilst the final joint shall be determined using geometric analysis.

A diagram defining the relevant parameters of the manipulator is given in Figure 3.

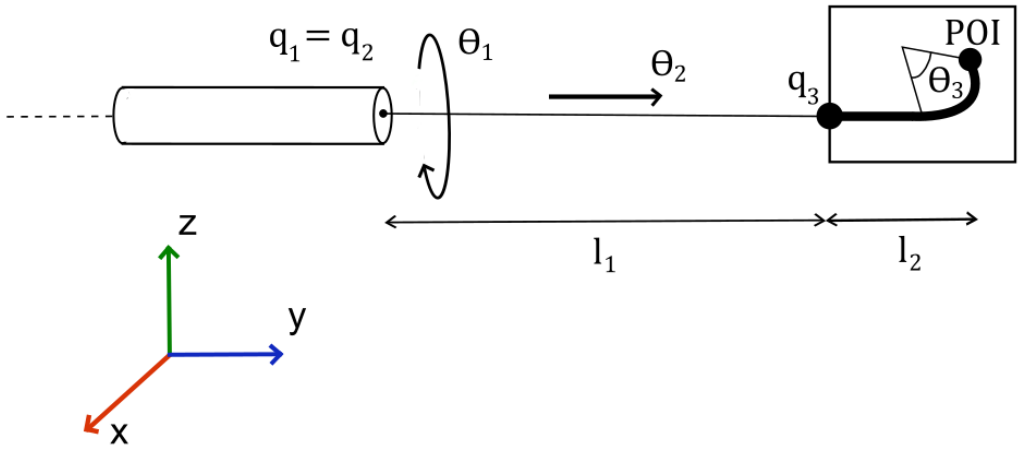


Figure 3. A kinematic scheme of the steerable catheter used in this study. The three degrees of freedom are (i) axial rotation about the y-axis (θ_1), (ii) prismatic insertion along the y-axis (θ_2), and (iii) constant-curvature bending of a 90 mm distal segment (θ_3). This 3-DoF layout mirrors the mechanism of commercial steerable sheaths used in aortic interventions and, by adopting the constant-curvature assumption, admits closed-form forward and inverse kinematics. The chosen segment lengths cover ∼95% of the reachable workspace for a 15–35 mm aortic radius while keeping the actuator count minimal.

The complete transformation is now described by Equation (7).

$$g_{\mathrm{st}}(\theta) = e^{\hat{\xi}_1\theta_1} e^{\hat{\xi}_2\theta_2} T_2^3 g_{\mathrm{st}}(0) \tag{7}$$

The transformation matrix T_2^3 represents the rigid-body transform that maps frame 2 to frame 3, corresponding to the bending segment.

Equation (7) is evaluated as

$$g_{\mathrm{st}}(\theta) = \begin{bmatrix} R(\theta) & p(\theta) \\ 0_{1\times 3} & 1 \end{bmatrix} \tag{8}$$

We use the same representations as for the previous transformation matrix. $R(\theta)$ can then be expressed as

$$R(\theta) = \begin{bmatrix} c_1c_3 & -c_1s_3 & s_1 \\ s_3 & c_3 & 0 \\ -c_3s_1 & s_1s_3 & c_1 \end{bmatrix} \tag{9}$$

and $p(\theta)$ as

$$p(\theta) = \begin{bmatrix} c_1\left(l_1 + \frac{l_2}{\theta_3}s_3\right) \\ \theta_2 + \left(\frac{l_2}{\theta_3}\left(1 - c_3\right)\right) \\ -s_1\left(l_1 + \frac{l_2}{\theta_3}s_3\right) \end{bmatrix} \tag{10}$$

The tip position combines the straight-segment length l_1 with the arc-length contribution $l_2 = 90$ mm.

Equation (8) now fully describes the transformation from base to end-effector.

2.2.2. Inverse Kinematics

The first joint is revolved about the y-axis. This will affect the rotation of the bending plane of the catheter. The second joint is prismatic along the y-axis. The third, the bending joint, has movement within the bending plane.

The prismatic joint is straightforward. An abstraction is shown in Figure 2 with $\theta = \frac{\pi}{2}$. Without derivation,

$$\theta_2 = p_{y_0} - p_y \tag{11}$$

Turning to joint 3, the geometric analysis yields functions that cannot be solved algebraically. Instead, the following transcendental function can be solved to determine the required joint angle.

$$f(\theta_3) = \frac{l}{\theta_3} \sin \theta_3 \tag{12}$$

To determine the solution to this equation, we require θ_3 such that

$$f(\theta_3) - p_y = 0 \tag{13}$$

The value or values (as there can be infinitely many solutions) that satisfy the above equation will also be the global minimiser or minimisers of the optimisation problem.

$$\min \| f(\theta_3) - p_y \|_2^2 \tag{14}$$

The transcendental equation for θ_3 is solved numerically (Newton–Raphson) to obtain the bending joint angle. For the catheter, this is assumed to be known. The C-Arm requires extra modelling to devise a method that allows for the determination of the required θ_3 for some position.

2.3. Fluoroscope Projection and Image Processing

Modelling the Projection

Each point on the catheter within the projection window is defined as the set $C = \{p_i \mid p_i \in \mathbb{R}^3\}$, where $i \in \mathbb{N}$ is the index of each point within the set. The projection is then the map $T_{\text{proj}} : \mathbb{R}^3 \to \mathbb{R}^2 \mid p_i \mapsto T_{\text{proj}}(p_i)$.

The transform T_{proj} can be expressed as the composition of the maps of the separate stages of the projection.

$$\begin{aligned} T_{\text{proj}} &= T_{\text{decomp}} \circ T_{\text{scale}} \circ T_{\text{trans}} \circ T_{\text{persp}} \circ T_{\text{rot}} \\ &= \begin{bmatrix} \alpha & 0 & \beta & 0 \\ -\frac{\sin\theta(t+b)}{t-b} & -\frac{2n}{r-l} & \frac{\cos\theta(t+b)}{t-b} & 0 \\ 0 & 0 & 0 & 0 \\ \sin\theta & 0 & -\cos\theta & 0 \end{bmatrix} \end{aligned} \tag{15}$$

where l , r, t, b denote the left, right, top, and bottom image-plane borders and n is the near-plane distance, in which

$$\alpha = \frac{2n\cos\theta - \sin\theta(r+l)}{r-l} \tag{16}$$

and

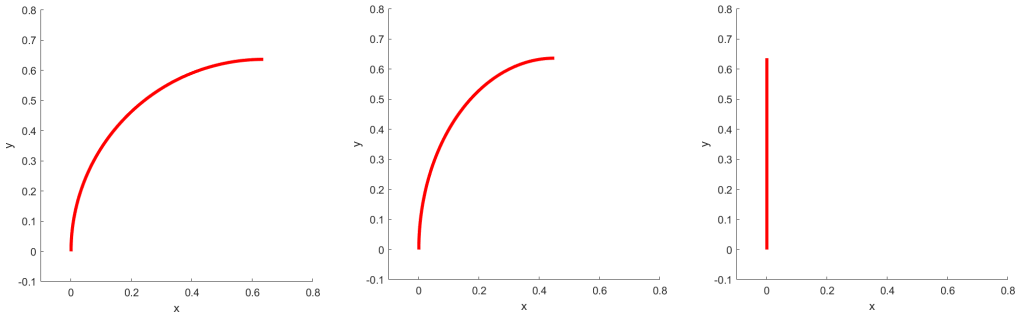
$$\beta = \frac{2n\sin\theta + \cos\theta(r+l)}{r-l} \tag{17}$$

In applying the transformation T_{proj} to every element in C, we acquire the set $C_P = \{T_{\text{proj}}(p_i) \mid T_{\text{proj}}(p_i) \in \mathbb{R}^2\}$, where $i \in \mathbb{N}$ is the index of each point within the set.

2.4. Idealised Projection and Baseline Image Pipeline

The algorithm in this section is solely intended to validate the control loop and therefore does not yet account for scatter, anatomical clutter, or quantum noise; these factors will be addressed in subsequent physical experiments.

In this context, it is crucial to determine the rotation of the bending plane, as it directly affects the perceived bending angle from a fixed viewpoint, as illustrated in Figure 4.



(**a**) 0 rad (**b**) $\frac{\pi}{4}$ rad (**c**) $\frac{\pi}{2}$ rad

Figure 4. Catheter tip of length 1 cm and bending angle $\frac{\pi}{2}$ rad for different angles of rotation.

Angle estimation allows one to detect this change in orientation. The projection model gives us an image of the form shown in Figure 5. The pixel intensities are inverted to mimic the white-background, dark-catheter appearance of clinical fluoroscopy.



(a) (b)

Figure 5. (**a**) Synthetic fluoroscopic image generated by the projection model for a catheter bent to $\pi/2$ rad; pixel intensities are inverted to match the white-field contrast of clinical fluoroscopy. (**b**) Binary mask and 1-pixel skeleton obtained from (**a**) after threshold-based segmentation and morphological thinning; these features are subsequently used for circle fitting and bending-angle estimation.

It should be noted that, for this research, the artificial image is ideal. The effects of noise, blurring, and additional objects within the image are ignored.

To discern whether a pixel belongs to the background or the catheter, a process known as segmentation must be applied. Regions are formed in the image, with pixels belonging to objects or a specific part of an object within that image.

If we let R represent the entire spatial region occupied by the image,

$$R = R_1 \cup R_2 \mid R_1 \cap R_2 = \emptyset \tag{18}$$

in which R_1 represents the pixels belonging to the catheter and R_2 those belonging to the background.

As the ideal image is simple, thresholding is adequate to segment the image. A histogram of the image's pixel intensities is created. Thresholds are then chosen to segment the image into the desired regions of interest. Let I_T represent the pixel intensity threshold and $f(x,y)$ the pixel intensity within the image. We can then define $g(x,y)$ as the binary value of that pixel after the threshold has been applied.

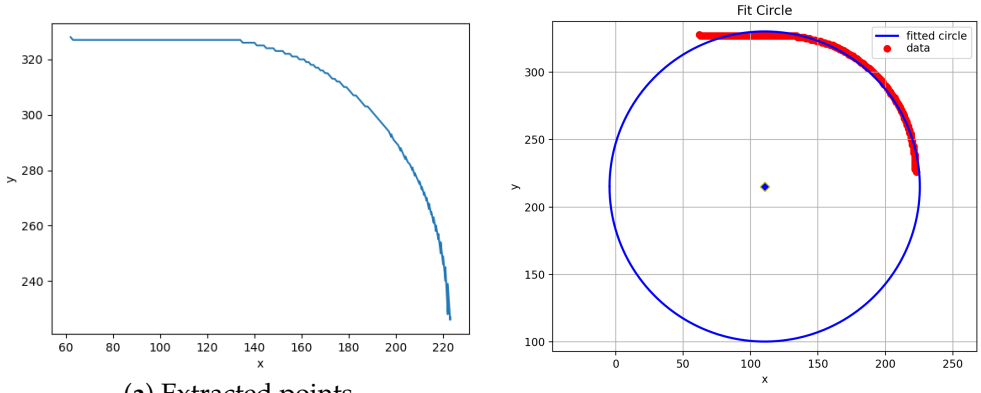
$$g(x,y) = \begin{cases} 1 & f(x,y) \geq I_T \\ 0 & f(x,y) < I_T \end{cases} \tag{19}$$

We can reduce the binary objects to a 1-pixel-wide representation to simplify feature extraction. This is called skeletonisation. It entails making successive passes of the image to identify pixel borders, which are removed on the condition that the connectivity of the corresponding object is not broken. The image in Figure 5 results from all this combined processing.

Extracting the location of each pixel with the binary value corresponding to region R_1 yields the set C_P. Figure 6 results from plotting each element of the set.

The bending part of the catheter is well-modelled as the segment of a circle. One can obtain the bending angle using the equations of an arc length, namely, $l = r\theta$. l is a known quantity; hence, a method of obtaining r is required.

Acquiring the circle corresponding to the segment acting as the flexible portion of the catheter can be performed using a fitting algorithm. This comprises solving a minimisation problem to obtain the best estimate of a circle that fits all the points in C_P. An estimate of the angle follows from this.



(**a**) Extracted points (**b**) Circle fitting result

Figure 6. (**a**) Points extracted from the artificial image after image processing; (**b**) fitted circle result based on the extracted points.

For the vectors belonging to the set C_P, we define the equation of an ideal circle.

$$(x_i - x_c)^2 + (y_i - y_c)^2 = r^2 \tag{20}$$

where $i \in \mathbb{N}$ is the index of a vector belonging to C_P. Rewriting the expression,

$$ax_i + by_i + c = x_i^2 + y_i^2 \tag{21}$$

in which

$$\begin{aligned} a &= 2x_c \\ b &= 2y_c \\ c &= r^2 - x_c^2 - y_c^2 \end{aligned} \tag{22}$$

For every vector in C_P, the whole system can be written in matrix form. Let n be the number of vectors belonging to the set C_P. Then,

$$\begin{bmatrix} x_1 & y_1 & 1 \\ x_2 & y_2 & 1 \\ \cdots & \cdots & \cdots \\ x_n & y_n & 1 \end{bmatrix} \cdot \begin{bmatrix} a \\ b \\ c \end{bmatrix} = \begin{bmatrix} x_1^2 + y_1^2 \\ x_2^2 + y_2^2 \\ \cdots \\ x_n^2 + y_n^2 \end{bmatrix} \tag{23}$$

$$Ax = b$$

where $A \in \mathbb{R}^{n\times 3}$, $x \in \mathbb{R}^3$, and $b \in \mathbb{R}^n$. The optimal solution to this inconsistent system of equations is given by

$$\begin{aligned} \hat{x} &= \left(A^T A\right)^{-1} A^T b \\ &= \begin{bmatrix} a \\ b \\ c \end{bmatrix} \end{aligned} \tag{24}$$

where $\hat{x} \in \mathbb{R}^3$. Rearranging the original expression for a, b, and c,

$$\begin{aligned} x_c &= \frac{a}{2} \\ y_c &= \frac{b}{2} \\ r &= \frac{\sqrt{4c + a^2 + b^2}}{2} \end{aligned} \tag{25}$$

We obtain the parameters of the best-fitting circle for C_P.

The results of applying the fitting algorithm to the points displayed in Figure 6a are seen in Figure 6b.

3. C-Arm Control Strategy Design

Each control cycle proceeds as follows: the fluoroscope acquires an image; the bending angle $\hat{\theta}_{\text{bend}}$ is extracted; the resulting angle error is mapped, via the C-arm Jacobian, to a correction $\Delta\theta_3$ of joint 3; and the updated pose is applied to the next frame. It is assumed that the system dynamics are sufficiently regulated, with "control" herein referring specifically to the high-level management of the manipulator kinematics. Within this framework, the maintenance of an optimal camera position relative to the catheter tip, within its bending plane, is achieved solely through the inverse kinematics of the C-arm. The catheter tip position—obtained by methods presumed to be available—is directly integrated as an input into the kinematic models, thereby enabling the dynamic adjustment of the C-arm manipulator configuration in response to the catheter's insertion and bending movements. Figure 7 presents a schematic representation of this control strategy.

It is important to note that the rotation of the catheter relative to the fluoroscope's perspective introduces ambiguity in angle estimation. Specifically, the "actual" angle (or best estimate) is defined as the maximum angle perceived by the estimator. As the catheter rotates, an illusion of an increasing bending radius arises, which in turn leads to a reduction in the estimated bending angle.

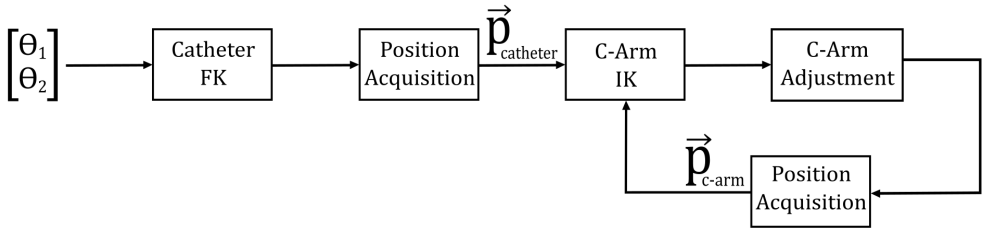


Figure 7. A block diagram for C-arm position control within the bending plane, where θ_1 and θ_2 denote the angles of the first and second joints of the catheter, respectively.

The rotation of the catheter's third joint is continuous, closed, and bounded within the interval $[0, 2\pi]$. Consequently, the extreme value theorem can be applied. Let f be a function representing the estimated angle for a given orientation of the catheter. Since f is continuous, closed, and bounded on the interval $[0, 2\pi]$, it follows that

$$f(c) \geq f(x) \geq f(d) \quad \forall x \in [0, 2\pi], \tag{26}$$

where $c, d \in \mathbb{R}$.

This theoretical foundation facilitates the development of a search algorithm that enables the C-arm to ascertain its optimal position. Initially, the angle estimator defines the current perceived angle. Subsequently, the C-arm's third joint is rotated both to the left and right of the current angle, with the perceived angles at these positions being compared to the current value. Upon detecting an increase in the perceived angle in one direction, the C-arm continues rotating and re-estimating the angle until the estimation begins to decline. The maximum angle perceived prior to the decline is then taken as the optimal (maximum perceived) angle, and the C-arm defines its operational position accordingly. Figure 8 illustrates the control method for optimal perspective tracking.

Each control cycle proceeds as follows: the fluoroscope acquires an image; the bending angle $\hat{\theta}_{\text{bend}}$ is extracted; the resulting angle error is mapped, via the C-arm Jacobian, to a correction $\Delta\theta_3$ of joint 3; and the updated pose is applied for the next frame.

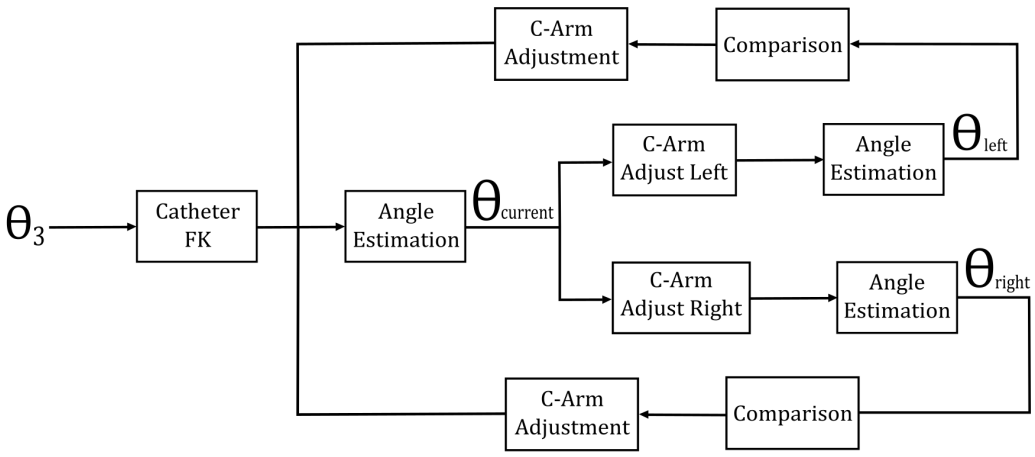


Figure 8. A block diagram for optimal perspective tracking of the C-arm, while $\Delta\theta_3$ is the incremental correction commanded at each cycle.

Moreover, full system automation is achieved by incorporating an additional preliminary step into the block diagram shown in Figure 7. By employing the inverse kinematics of the catheter manipulator, the system is enabled to follow a preplanned trajectory with high precision, thereby further enhancing operational efficiency and control accuracy.

4. Testing the Proposed System

4.1. Simulator

We prove the feasibility of the proposed system by creating a simulation test bench. This aims to showcase the validity of the models and control and ultimately the effectiveness of the design.

Figure 9 is an image of the simulation environment. Both systems are modelled, and an aorta is also visible. The catheter is controlled through joint angle inputs. The window in the bottom right corner displays the projection from the fluoroscope.

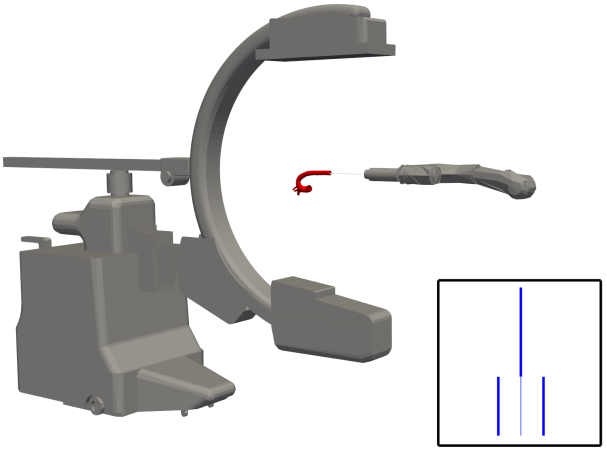


Figure 9. An overview of the system within the simulation environment.

Figure 10 depicts the bending joint for various angle inputs. The endpoint is also identified.

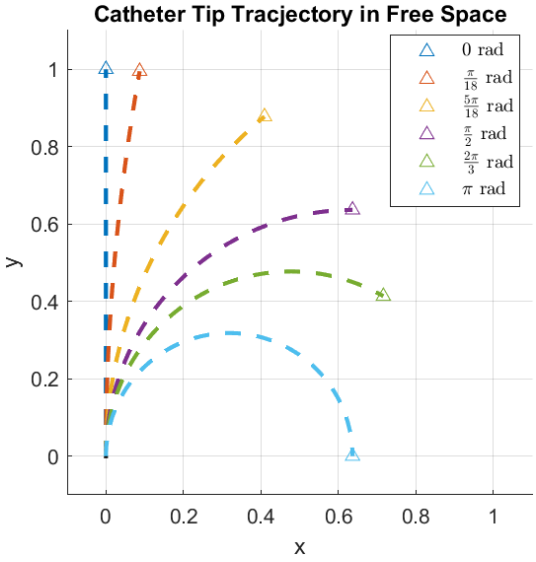


Figure 10. A plot of the catheter's bending joint for various angles and a length of 1. A triangle marks the endpoint.

The validity of this model within the simulation environment is shown in Figure 11.

Under noise-free conditions the projection model recovers the expected geometric projection. Changing the position of the C-Arm receiver relative to the aorta changes the angle at which it is perceived, as shown in Figure 12.

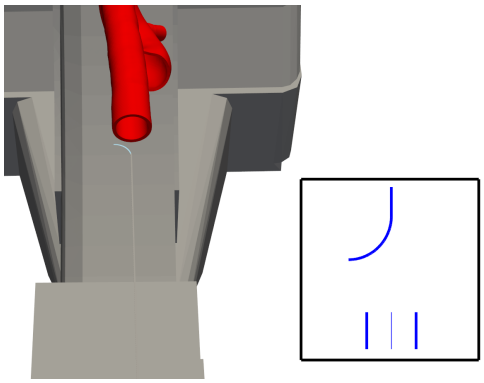
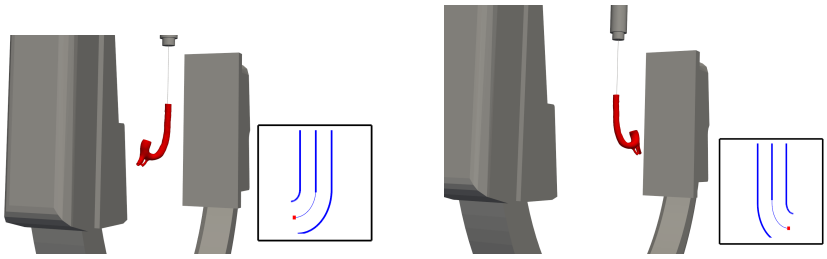


Figure 11. An image of the simulator depicting the bending joint and its projection for a bending angle of $\frac{\pi}{2}$ rad.



(**a**) (**b**)

Figure 12. (**a**) Orthogonal projection of the aortic bend with the C-arm detector perpendicular to the bending plane. (**b**) Oblique projection after re-orienting the detector away from orthogonality, in which the same aortic bend appears flatter due to geometric foreshortening.

Figure 13 displays the result of the searching algorithm and the automated catheter insertion. The camera seeks the optimal position (approximately orthogonal to the bending plane of the aorta), and the catheter calculates the correct joint angles to reach the target.

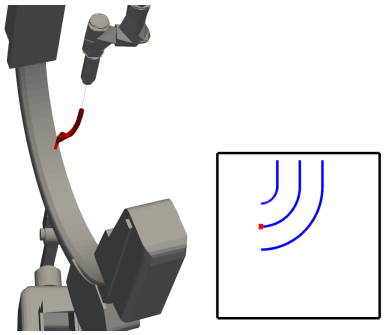


Figure 13. An example of automated catheter insertion; the target is marked in red.

4.2. Evaluation of Manipulator Kinematics

Further validation of the accuracy of the automated catheter insertion methods is accomplished by comparing the actual and calculated bending angles. Table 1 lists the actual and calculated angles. The percentage error is also included.

The percentage error for a bending angle of 10 deg is most noticeable. For bending angles below 13 deg, the minimisation algorithm used in the inverse kinematics calculations yields a near-zero solution. Initial speculation would suggest that the starting point of the algorithm is incorrect for small angles. This, however, needs further investigation. For angles above 13 deg, the inverse kinematics method performs with acceptable degrees of error. Catheter insertion, therefore, is only possible for targets with bending angles $>$ 13 deg.

Table 1. Validation of bending joint's inverse kinematics.

Actual Angle (°)	Calculated Angle (°)	Percentage Error (%)
10	9.70	3.00
20	19.97	0.15
30	29.96	0.13
40	39.94	0.15
50	49.93	0.14
60	59.91	0.15
70	69.90	0.14
80	79.88	0.15
90	89.87	0.14

4.3. Assessment of Catheter Angle Estimation

A similar analysis is performed to validate the performance of the angle estimator, the results of which are given in Table 2 below.

Table 2. Validation of angle estimator.

Actual Angle (°)	Estimated Angle (°)	Percentage Error (%)
10	9.36	6.40
20	19.40	3.00
30	29.87	0.43
40	38.98	2.55
50	48.85	2.30
60	60.36	0.60
70	69.98	0.03
80	80.54	0.68
90	89.07	1.03

5. Discussion

This section describes the simulation environment created to test and validate the feasibility of the proposed dual-manipulator control scheme. It demonstrates how the forward and inverse kinematics, along with the projection model and image processing pipeline, function together under realistic conditions. Quantitative evaluations of accuracy—such as the catheter's bending angle estimation and the inverse kinematics solutions—confirm the viability of the approach and reveal areas for refinement.

5.1. Summary and Reflection

This research aimed to demonstrate a method of coordinating multiple medical devices in a catheter insertion procedure by utilizing two robotic manipulators. Through basic kinematics, one manipulator achieved rudimentary C-arm tracking of the catheter within its bending plane. Meanwhile, a mathematical formulation of the fluoroscope's projection enabled the creation of artificial images, from which the bending angle was estimated using image processing. A search algorithm then identified the optimal C-arm position relative to the catheter, defined here as *"the position at which the 'actual' angle (or best estimate) is perceived angle by the estimator "*, corresponding to the maximum estimated angle. Additionally, a path-tracking algorithm was employed to automate the insertion procedure fully. A simulation test bench verified the feasibility of these concepts, examining both angle-estimation accuracy and inverse kinematics performance.

Reflecting on the necessity of this approach, one must acknowledge potential drawbacks such as longer operating times and higher costs. However, such a system may help

limit surgeons' radiation exposure. Methods presented by De Silva et al. [23] propose virtual fluoroscopy to pre-determine positioning, ultimately reducing procedure duration and radiation levels. The bilateral controller described here could potentially reduce or even obviate the need for direct C-arm operation. Concurrently, Kausch et al. [20] implement a computer algorithm to automate C-arm positioning, although it relies on a "pre-scan" of the patient and is therefore less suited to continuously changing scenarios. Considering existing technologies presented by Matthäus et al. [24] and Namrata et al. [25], it becomes clear that more complex anatomical structures may challenge oversimplified models. The present work employs relatively straightforward manipulator assumptions, yet the core bilateral control scheme remains applicable even under greater realism. What may shift is the path-tracking aspect, given that real aortas typically deviate from the ideal shapes assumed in the simulator. Further advanced image processing methods, like those presented by Alam [26], for extracting the true centre-line of a real aorta would produce a more robust system.

5.2. The Development of a Realistic Application

Building on the above reflections, the following points outline key requirements for developing a more realistic application of the proposed system:

- Increased complexity in the manipulator model.
- Introduction of noise and blurring effects to yield less idealised images.
- More realistic modelling of the aorta.
- Additional image processing techniques.

In practice, the manipulators will likely possess more degrees of freedom, and the flexible joint may exhibit hysteresis that demands dedicated modelling. Further image processing would also be necessary to determine the catheter's position in the global frame, differentiate between straight and bending regions, and locate the aorta's central lumen. Moreover, imposing boundaries on the C-arm's permissible motion could clarify how the controller behaves in confined spaces.

In addition, future work will explore the integration of machine learning and deep learning techniques with biosignals [27–29], such as the muscular activity of clinicians, to enable more adaptive and intelligent control strategies, thereby further enhancing the completeness and usability of the system.

5.3. Optimisation Potential and Limitations of Proposed System

5.3.1. Optimisation Potential

No explicit attention has yet been paid to optimizing the control approach. Potential avenues for improvement include

- Adjusting the C-arm's step size;
- Minimizing the steps required for optimal positioning;
- Reducing control effort while maintaining performance;
- Constraining the catheter's maximum deviation from a planned path during automatic insertion.

Improving efficiency in these areas may reduce overall control demands and boost precision. Consequently, the risk of path deviation could diminish, although this would likely depend on refined path-planning algorithms as well.

5.3.2. System Limitations

For small bending angles, automated catheter insertion currently suffers from significant inaccuracy since the inverse kinematics method may yield large errors below around 13°. Given that the catheter is narrower than the aorta, minor deviations at low angles

are unlikely to cause wall collisions. Nonetheless, introducing an improved initial-guess strategy could better guide the root-finding algorithm.

Furthermore, in clinical endovascular procedures, vessels can sometimes feature curvatures greater than 90°, posing additional challenges for catheter navigation. Our current study and simulation models have not yet been validated for such extreme bends. Future work will therefore incorporate a more robust kinematic model and imaging strategy to address higher bending angles, better reflecting real-world vascular complexities.

Lastly, the impact of latency in hardware communication has yet to be modeled. This gap invites questions such as how automatic and manual insertion times compare and how rapidly the C-arm can reposition itself when the catheter's shape changes. Addressing these issues will be central to understanding the bilateral control framework's performance in practical surgical scenarios and may encourage broader adoption of the proposed methods.

6. Conclusions

This paper presented a potential approach for coordinating multiple medical devices via a bilateral control scheme, leveraging a flexible catheter's position and bending angle to automate the control of a C-arm fluoroscope. Such coordination may not only streamline the catheter insertion process but also help mitigate radiation risks for both surgeon and patient. By incorporating path tracking for catheter navigation, this control scheme aims to enable full procedural automation, although further testing in realistic scenarios is still recommended.

Analytical methods were used to derive inverse and forward kinematics for both systems, and the resulting transformation matrices were detailed. Forward kinematics relied on a series of linear transformations from base to end-effector, while inverse kinematics combined geometric analysis with function minimisation. Although the kinematic models proved sufficient for manual catheter control, inaccuracies arose at small bending angles during automatic insertion, leading to slight deviations from the intended path.

Additionally, the fluoroscope projection was modeled to generate artificial images, from which bending angles were inferred through image processing. Recognizing that perceived bending angles vary with catheter orientation, a search-based approach was implemented to optimise the fluoroscope's vantage point. This estimator showed promising accuracy, thus supporting a robust C-arm positioning strategy.

A test bench simulator was developed to validate the system models and to illustrate how the bilateral controller might operate in practice. These outcomes suggest that the proposed concept is technically feasible, offering a new perspective on automating catheter insertion procedures. Nonetheless, further refinements—particularly for real-world surgical environments—would be instrumental in advancing this framework from simulation to clinical application.

Author Contributions: Conceptualisation, G.Y.W.; Data curation, K.N.; Formal analysis, G.Y.W.; Methodology, G.Y.W. and D.S.; Project administration, K.N.; Software, G.Y.W.; Supervision, K.N.; Validation, G.Y.W. and D.S.; Visualization, D.S.; Writing—original draft, G.Y.W., D.S. and K.N.; Writing—review and editing, D.S. and K.N.; D.S. and G.Y.W. contributed equally to this work and share first authorship. All authors have read and agreed to the published version of the manuscript.

Funding: This research received no external funding.

Data Availability Statement: Data is contained within the article.

Conflicts of Interest: The authors declare no conflicts of interest.

References

1. Lee, A.; Baker, T.S.; Bederson, J.B.; Rapoport, B.I. Levels of Autonomy in FDA-Cleared Surgical Robots: A Systematic Review. *NPJ Digit. Med.* **2024**, *7*, 49. [CrossRef] [PubMed]
2. Samprón, N.; Lafuente, J.; Presa-Alonso, J.; Ivanov, M.; Hartl, R.; Ringel, F. Advancing Spine Surgery: Evaluating the Potential for Full Robotic Automation. *Brain Spine* **2025**, *5*, 104232. [CrossRef] [PubMed]
3. Zhou, X.; Chen, Y.; Miao, G.; Guo, Y.; Zhang, Q.; Bi, J. Computer-aided robotics for applications in fracture reduction surgery: Advances, challenges, and opportunities. *iScience* **2025**, *28*, 111509. [CrossRef] [PubMed]
4. Dagnino, G.; Kundrat, D. Robot-assistive minimally invasive surgery: Trends and future directions. *Int. J. Intell. Robot. Appl.* **2024**, *8*, 812–826. [CrossRef]
5. Kumar, R.; Choudhary, R.K.; Archana; Yadav, N.K. Calibration of Medical Devices: Method and Impact on Operation Quality. *Int. J. Pharm. Sci.* **2024**, *16*, 1. [CrossRef]
6. Legrand, J.; Niu, K.; Qian, Z.; Denis, K.; Vander Poorten, V.; Van Gerven, L.; Vander Poorten, E. A Method Based on 3D Shape Analysis Towards the Design of Flexible Instruments for Endoscopic Maxillary Sinus Surgery. *Ann. Biomed. Eng.* **2021**, *49*, 1534–1550. [CrossRef]
7. Schols, R.M.; Connell, N.J.; Stassen, L.P.S. Near-Infrared Fluorescence Imaging for Real-Time Intraoperative Anatomical Guidance in Minimally Invasive Surgery: A Systematic Review of the Literature. *World J. Surg.* **2015**, *39*, 1069–1079. [CrossRef]
8. Yang, S.; Xiao, D.; Geng, H.; Ai, D.; Fan, J.; Fu, T.; Song, H.; Duan, F.; Yang, J. Real-Time 3D Instrument Tip Tracking Using 2D X-Ray Fluoroscopy With Vessel Deformation Correction Under Free Breathing. *IEEE Trans. Biomed. Eng.* **2025**, *72*, 1422–1436. [CrossRef]
9. Patel, B.; Jadon, J.S. Advancements in Image-Guided Surgical Procedures: Enhancing X-Ray Images, Cross Marker Classification, and C-Arm Rotation Detection. In *Advances in Data and Information Sciences*; Tiwari, S., Trivedi, M.C., Kolhe, M.L., Singh, B.K., Eds.; Springer: Singapore, 2024; pp. 169–178.
10. Rowantree, S.; Currie, C. Orthopaedic surgeons' knowledge and practice of radiation safety when using fluoroscopy during procedures: A narrative review. *Radiography* **2024**, *30*, 274–281. [CrossRef]
11. Videira, S.; Rodrigues, M.A.; da Silva, M.V. Worker's exposure to radiation in fluoroscopy, assessing and instruments: A systematic literature review. *Prev. Med.* **2024**, *182*, 107913. [CrossRef]
12. Watanabe, S.; Nakanishi, K.; Mura, M.; Yutori, A.; Hitomi, G.; Uchino, K.; Iba, H.; Sugimoto, Y.; Mitani, S. Investigation of Radiation Exposure of Medical Staff During Lateral Fluoroscopy for Posterior Spinal Fusion Surgery. *J. Clin. Med.* **2024**, *13*, 6442. [CrossRef] [PubMed]
13. Daryoush, J.R.; Lancaster, A.J.; Frandsen, J.J.; Gililland, J.M. Occupational Hazards to the Joint Replacement Surgeon: Radiation Exposure. *J. Arthroplasty* **2022**, *37*, 1464–1469. [CrossRef] [PubMed]
14. Schreiner, M.; Egger, P.; Neururer, S.; Luger, F.; Primavesi, F.; Gföller, P.; Braun, R.; Gassner, E.-M.; Bale, R.; Schicho, A. RAY-POS: A LIDAR-based assistance system for intraoperative C-arm repositioning. *Int. J. Comput. Assist. Radiol. Surg.* **2022**, *17*, 681–689. [CrossRef]
15. Uneri, A.; De Silva, T.; Stayman, J.W.; Khanna, A.J.; Siewerdsen, J.H. Virtual fluoroscopy for intraoperative C-arm positioning and radiation exposure reduction. *Med. Phys.* **2018**, *45*, 2320–2332. [CrossRef]
16. Zhang, L.; Zuo, J.; Wang, K.; Jiang, T.; Gu, S.; Xu, L.; Zhang, Y. An advanced robotic system incorporating haptic feedback for precision cardiac ablation procedures. *Sci. Rep.* **2025**, *15*, 6839. [CrossRef]
17. Yang, G.-Z.; Cambias, J.; Cleary, K.; Daimler, E.; Drake, J.; Dupont, P.E.; Hata, N.; Kazanzides, P.; Martel, S.; Patel, R.V.; et al. Medical robotics—Regulatory, ethical, and legal considerations for increasing autonomy. *Sci. Robot.* **2017**, *2*, eaam8638. [CrossRef]
18. Gomez-Paz, S.; King, P.; Gomez, A.; Grandhi, R. Exploring Robotic Advances, Applications, and Challenges in Neuroendovascular Surgery: A Scoping Review of the CorPath GRX System. *Interv. Neuroradiol.* **2024**. [CrossRef]
19. Najafi, G.; Kreiser, K.; Abdelaziz, M.E.M.K.; Hamady, M.S. Current State of Robotics in Interventional Radiology. *Cardiovasc. Intervent. Radiol.* **2023**, *46*, 549–561. [CrossRef]
20. Kausch, L.; Thomas, S.; Kunze, H.; Privalov, M.; Vetter, S.; Franke, J.; Mahnken, A.H.; Maier-Hein, L.; Maier-Hein, K. Toward Automatic C-Arm Positioning for Standard Projections in Orthopedic Surgery. *Int. J. Comput. Assist. Radiol. Surg.* **2020**, *15*, 1095–1105. [CrossRef]
21. Caccianiga, G.; Sharon, Y.; Javot, B.; Polikovsky, S.; Ergün, G.; Capobianco, I.; Mihaljevic, A.L.; Deguet, A.; Kuchenbecker, K.J. Open-Source Multi-Viewpoint Surgical Telerobotics. *arXiv* **2025**, arXiv:2505.11142.
22. Schleer, P.; Drobinsky, S.; de la Fuente, M.; Radermacher, K. Toward Versatile Cooperative Surgical Robotics: A Review and Future Challenges. *Int. J. Comput. Assist. Radiol. Surg.* **2019**, *14*, 1673–1686. [CrossRef] [PubMed]
23. De Silva, T.; Punnoose, J.; Uneri, A.; Goerres, J.; Jacobson, M.; Ketcha, M.D.; Manbachi, A.; Vogt, S.; Kleinszig, G.; Khanna, A.J.; et al. C-Arm Positioning Using Virtual Fluoroscopy for Image-Guided Surgery. In *Medical Imaging 2017: Image-Guided Procedures, Robotic Interventions, and Modeling*; SPIE: Bellingham, WA, USA, 2017; Volume 10135. [CrossRef]

24. Binder, N.; Matthäus, L.; Burgkart, R.; Schweikard, A. A Robotic C-Arm Fluoroscope. *Int. J. Med. Robot. Comput. Assist. Surg.* **2005**, *1*, 108–116. [CrossRef] [PubMed]
25. Nayar, N.U.; Qi, R.; Desai, J.P. Towards the Design and Development of a Robotic Transcatheter Delivery System for Mitral Valve Implant. *IEEE Trans. Med. Robot. Bionics* **2022**, *4*, 922–934. [CrossRef] [PubMed]
26. Alam, S.; Rahman, S.U.; Khalil, A.; Alam, F.; Alam, K.; Hadi, A. An Enhanced Algorithm for Image Processing Based Catheter Selection During Right Coronary Angiography. *J. Saidu Med. Coll.* **2021**, *11*, 18–23. [CrossRef]
27. Peng, Y.; Yang, X.; Li, D.; Ma, Z.; Liu, Z.; Bai, X.; Mao, Z. Predicting flow status of a flexible rectifier using cognitive computing. *Expert Syst. Appl.* **2025**, *264*, 125878. [CrossRef]
28. Peng, Y.; Sakai, Y.; Nakagawa, K.; Funabora, Y.; Aoyama, T.; Yokoe, K.; Doki, S. Funabot-Suit: A bio-inspired and McKibben muscle-actuated suit for natural kinesthetic perception. *Biomim. Intell. Robot.* **2023**, *3*, 100127. [CrossRef]
29. Lan, B.; Krijnen, G.; Stramigioli, S.; Niu, K. Deciphering Muscular Dynamics: A Dual-Attention Framework for Predicting Muscle Contraction from Activation Patterns. *IEEE J. Biomed. Health Inform.* **2025**, 1–14. [CrossRef]

Disclaimer/Publisher's Note: The statements, opinions and data contained in all publications are solely those of the individual author(s) and contributor(s) and not of MDPI and/or the editor(s). MDPI and/or the editor(s) disclaim responsibility for any injury to people or property resulting from any ideas, methods, instructions or products referred to in the content.